Article

Conversion of non-van der Waals solids to 2D transition-metal chalcogenides

Zhiguo Du[1], Shubin Yang[1]*, Songmei Li[1], Jun Lou[2], Shuqing Zhang[3], Shuai Wang[1], Bin Li[1], Yongji Gong[1], Li Song[4], Xiaolong Zou[3] & Pulickel M. Ajayan[2]*

Although two-dimensional (2D) atomic layers, such as transition-metal chalcogenides, have been widely synthesized using techniques such as exfoliation[1–3] and vapour-phase growth[4,5], it is still challenging to obtain phase-controlled 2D structures[6–8]. Here we demonstrate an effective synthesis strategy via the progressive transformation of non-van der Waals (non-vdW) solids to 2D vdW transition-metal chalcogenide layers with identified 2H (trigonal prismatic)/1T (octahedral) phases. The transformation, achieved by exposing non-vdW solids to chalcogen vapours, can be controlled using the enthalpies and vapour pressures of the reaction products. Heteroatom-substituted (such as yttrium and phosphorus) transition-metal chalcogenides can also be synthesized in this way, thus enabling a generic synthesis approach to engineering phase-selected 2D transition-metal chalcogenide structures with good stability at high temperatures (up to 1,373 kelvin) and achieving high-throughput production of monolayers. We anticipate that these 2D transition-metal chalcogenides will have broad applications for electronics, catalysis and energy storage.
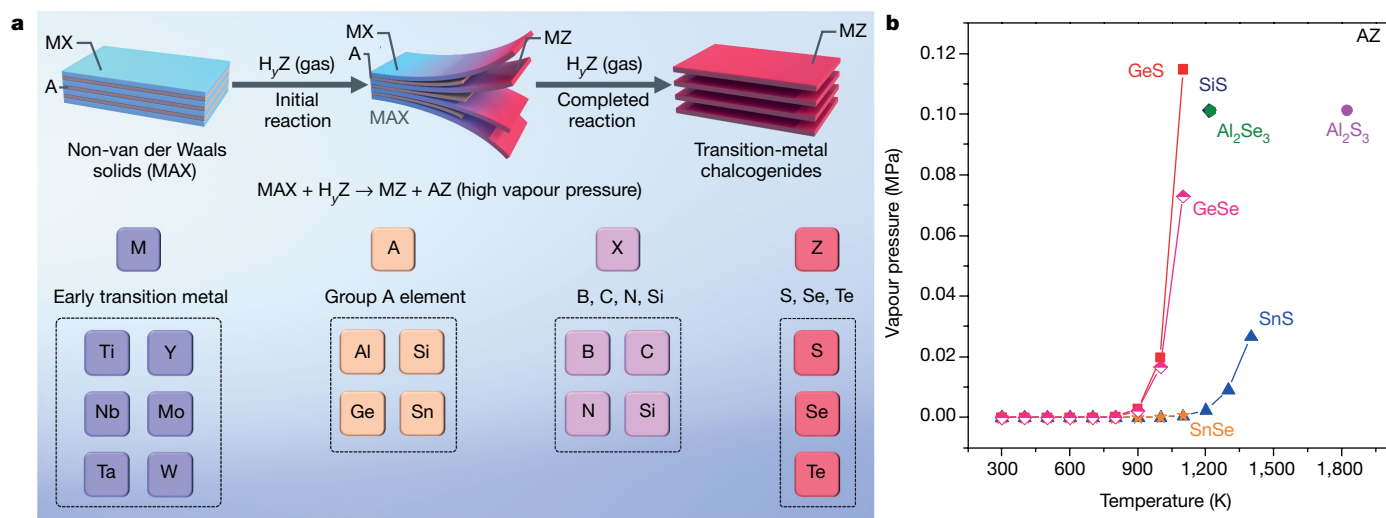
Two-dimensional (2D) atomic-layer crystals have demonstrated many unique physical and chemical properties as well as broad applications in electronics[2], sensors[5], catalysts[9] and batteries[10,11]. Generally, 2D structures such as graphene, boron nitride and transition-metal sulfides can be produced via a top-down approach, that is, by directly exfoliating the vdW counterparts through mechanical[3], liquid-phase[1] and electrochemical procedures[2]. In this manner, various vdW materials—such as metal oxides[12], hydroxides[13] and topological insulators[14]—can also be synthesized, enriching the 2D family of materials. In these 2D vdW nanocrystals, the elemental compositions, stoichiometric ratios and structural phases are usually inherited from their parent bulk counterparts, although 2D nanocrystals with phase-specific structures such as 1T and 2H phases are difficult to synthesize selectively[6,7]. Here we demonstrate an efficient topological conversion of non-vdW solids such as transition-metal carbides and nitrides under chalcogen vapours to 2D vdW transition-metal chalcogenide layers with identified 2H/1T phases, good stability at high temperatures (<1,373 K) and achieving high-throughput production of monolayers. We anticipate that the resultant transition-metal chalcogenide layers with favourable features would have broad applications for electronics, energy storage and conversions.

In the past decade, some unusual 2D nanocrystals have emerged from non-vdW solids such as haematite[15] or bulk layered transition-metal carbides and nitrides[16], namely MAX phases, greatly increasing the number of 2D material compositions accessible. In particular, the non-vdW MAX phases—where M represents a transition-metal element, A usually represents an element from groups 13–16 of the periodic table and X is carbon or nitrogen—have predominantly mixed covalent or ionic M–X bonds and metallic M–A bonds[17,18]. Because the M–A bonds are more chemically active than the M–X bonds, A species in MAX phases can be extracted using highly reactive solvents (hydrogen fluoride and strong bases)[16,19], allowing few-layer-thick 2D transition-metal carbides, carbonitrides and nitrides—called MXenes—to be created. These 2D nanocrystals are usually terminated with defects and surface terminations of -OH, -O, -F or -Cl[20–22]. Owing to the very close atomic packing and strong chemical bonds in non-vdW solids, it remains a challenge to convert them to 2D nanocrystals with abundant exposed surfaces and identified phases.

Here we demonstrate an efficient strategy that enables us to convert a family of non-vdW bulk solids such as MAX phases to 2D transition-metal chalcogenides with well-defined phases. As depicted in Fig. 1a, under chalcogen-containing vapours (H_yZ, where Z represents sulfur, selenium or tellurium and y is 0 or 2) at high temperatures, non-vdW MAX phases and transition-metal borides, silicides and carbides (Supplementary Fig. 1) have high activities. In particular, the active M–A bonds in MAX phases react easily with chalcogen-containing gases, resulting in products of AZ and MZ compositions. Such reactions must produce an AZ intermediate product at high vapour pressure, which would allow rapid evaporation rates, thus boosting the continuous reaction into the bulk of the reactant material. Thermodynamically, if the reaction temperature were high enough, all the post-transition-metal A (Si, Al, Sn, Ge) species in MAX phases could be transformed to metal chalcogenide gases (Supplementary Figs. 2–5), which facilitates the conversion of MAX phases to 2D nanostructures. As an example, based on temperature–vapour pressure relationships (Fig. 1b and Supplementary Fig. 6)[23,24], germanium chalcogenides (GeS, GeSe)

Fig. 1 | Schematic illustration of the conversion of non-vdW solids to 2D vdW transition-metal chalcogenides. a, Non-vdW solids such as MAX phases are progressively transformed to 2D transition-metal chalcogenides via a topological conversion reaction (MAX + H_yZ (gas) → MZ + AZ), in which M represents an early-transition-metal element, A is an element from groups 13–16, X is C, N, B or Si, and Z refers to S, Se and Te, associated with volatile AZ products. **b**, Temperature–vapour pressure relationships for various AZ substances.

have higher vapour pressures than other chalcogenide materials (SiS, Al_2S_3, SnS) at 1,073 K; from this we expect Ge-containing MAX phases to be easily converted to 2D transition-metal chalcogenides with vdW layers (Fig. 2c and Supplementary Fig. 7). According to the Clausius–Clapeyron equation[25] (see equation (1) in Methods), upon increasing the temperature further to more than 1,100 K, other Si-, Sn- and Al-containing MAX phases should also serve as precursors for the generation of 2D transition-metal chalcogenides (Supplementary Fig. 8), owing to the increased vapour pressures of the products at higher reaction temperatures. Using this principle, we have synthesized 13 transition-metal chalcogenides (Supplementary Tables 1 and 2), including 7 binary chalcogenides (based on the Ti-, Nb-, Mo- and Ta-containing MAX phases and MXenes), 5 heteroatom-doped chalcogenides with selected 2H phase or 1T phase and one composite (based on quaternary MAX phases). This demonstrates that our synthetic protocol is versatile, enabling the efficient conversion of a large number of non-vdW bulk solids to 2D transition-metal chalcogenides. Notably, although the resulting 2D structures are derived from bulk MAX phases, their compositions and stoichiometric ratios are very different from the parent compositions and are also different from other products commonly derived from MAX phases, such as MXenes[16,26].

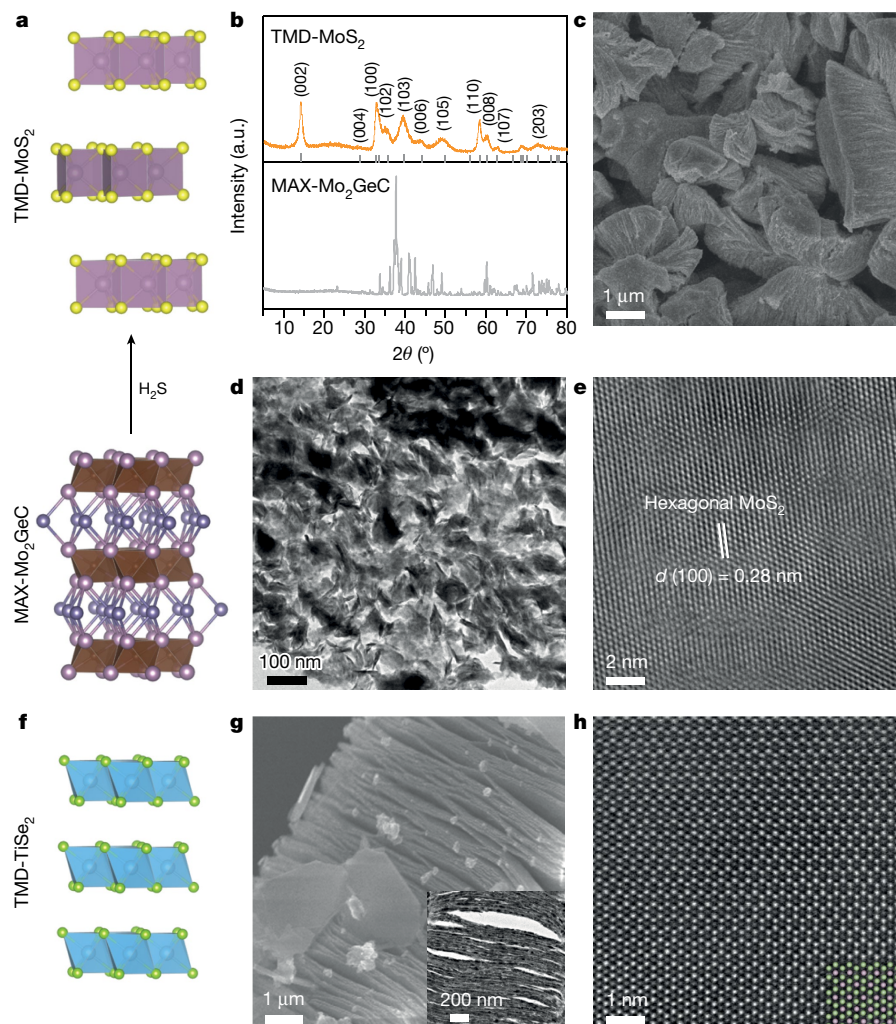## 2D transition-metal chalcogenides (2H/1T)

As a proof of concept, we produced 2D transition-metal dichalcogenide (TMD)-MoS_2 nanocrystals via engineering MAX-Mo_2GeC under hydrogen disulfide gas at 1,073 K (Fig. 2a; see Methods). X-ray diffraction patterns reveal the disappearance of Mo_2GeC peaks in the product (Fig. 2b). Instead, a series of diffraction peaks at 14.1°, 32.7°, 39.5° and 58.3° are well indexed to the (002), (100), (103) and (110) facets of hexagonal MoS_2 (according to Joint Committee on Powder Diffraction Standards (JCPDS) Card No. 37-1492), demonstrating the complete conversion and removal of Ge-layers from MAX-Mo_2GeC during our synthetic process. The resulting product exhibits uniform structure with largely extended spacing in the whole scanning electron microscope image (Fig. 2c and Supplementary Fig. 9), similar to those reported for expanded graphite and MXenes[16]. Transmission electron microscopy (TEM) (Fig. 2d and Supplementary Fig. 10) and high-resolution TEM (Fig. 2e) confirm clearly the highly exfoliated nanocrystals with a uniform interplanar spacing of 0.28 nm, in good agreement with the spacing between the (100) facets of 2H MoS_2 (ref. [2]).

To identify the interior structure of the resultant MoS_2, we conducted an ultrathin sectioning experiment. Many nanosheets with thicknesses from 0.4 nm to 4 nm are visible (Supplementary Fig. 11), indicating the co-existence of monolayers, bilayers and few layers in the sample. To inhibit the restacking of already-expanded 2D MoS_2 and improve the fraction of monolayers, the converted samples were rapidly transferred to a low-temperature zone during our synthetic process. Thus, the fraction of monolayer MoS_2 can be improved to 31% from 9% based on our standard conversion (Supplementary Figs. 12–16). Remarkably, when we directly converted thin non-vdW solid MXene-Mo_2CT_x in H_2S gas, the fraction of monolayer MoS_2 was up to about 91% (Supplementary Fig. 17). Raman spectra of the accordion-like MoS_2 (Supplementary Figs. 18 and 19) show two typical peaks at 379 cm^{-1} and 405 cm^{-1}, corresponding to the in-plane E_{2g}^1 and out-of-plane A_{1g} vibrational modes of 2H MoS_2 (Supplementary Fig. 67)[2], respectively. On the basis of thermodynamic considerations, by enhancing the reaction temperatures to more than 1,100 K, accordion-like $TiSe_2$ could also be derived from MAX-Ti_3SiC_2 by substituting H_2S with selenium vapour (Fig. 2f–h, Supplementary Figs. 20–24), owing to the high vapour pressure of the SiSe product at such high temperatures (Supplementary Fig. 4). An atomic-resolution scanning transmission electron microscopy (STEM) image of $TiSe_2$ (Fig. 2h) reveals the 1T superlattice with metal sites located at the centres of octahedral units. Such transformations suggest that our synthetic protocol can be generalized to convert non-vdW solids to vdW 2D nanocrystals with identified 2H/1T phases and high-throughput production of monolayers (Supplementary Figs. 25–36).

2D heteroatom-doped chalcogenides (2H/1T)

More than 70 ternary MAX phases[27] and some new quaternary MAX phases[28] such as $(W_{2/3}Y_{1/3})_2AlC$[29] and $(Ti_{1/2}Nb_{1/2})_2AlC$[30] have been explored, suggesting that it may be feasible to produce a series of transition-metal chalcogenides with multi-compositions via our topological conversion approach. One possibility is to produce accordion-like Y-doped WS_2 with the 2H phase (Fig. 3a, b and Supplementary Figs. 37–39) based on a $(W_{2/3}Y_{1/3})_2AlC$ precursor. After conversion with fast quenching, highly expanded accordion-like Y-doped WS_2 can be obtained, in which the fraction of monolayers is up to 27% (Supplementary Figs. 40–45).

Fig. 2 | Structural characterization of 2D transition-metal chalcogenides derived from MAX phases. a, Schematic illustration of the conversion of MAX-Mo_2GeC to accordion-like MoS_2 under H_2S gas at 1,073 K. **b**, X-ray diffraction patterns of MAX-Mo_2GeC and accordion-like MoS_2. **c**–**e**, Scanning electron microscope (**c**), sectional TEM (**d**) and high-resolution TEM (**e**) images of accordion-like MoS_2. **f**, Crystalline structure of 1T $TiSe_2$. **g**, Scanning electron microscope image and sectional TEM image (inset) of accordion-like $TiSe_2$, indicating its highly expanded structure. **h**, Atomic-resolution STEM image of $TiSe_2$ layers and the corresponding atomic configuration (inset) of the 1T phase. Purple and green balls represent Ti and Se atoms, respectively.

High-resolution elemental mapping images (Fig. 3f) reveal that Y species are mainly monoatomically dispersed into the layers, associated with a few Y clusters, possibly accounting for the many Y–S bonds present (Supplementary Fig. 46). A typical 2H structure is visualized in an aberration-corrected TEM image (Fig. 3c), consistent with X-ray diffraction (Supplementary Fig. 38) and Raman analysis (Fig. 3h), indicating that the heteroatoms remain stable within the host 2D transition-metal chalcogenide structure. To further verify the Y–S bonds in Y-doped WS_2, we conducted X-ray absorption near-edge fine structure (XANES) spectroscopy measurements. In the case of Y-doped WS_2, the absorption edge in Y K-edge XANES spectra (Fig. 3i) is close to that of yttrium sulfide, suggesting that the Y is in the sulfide state. The Fourier transform spectra resulting from the analysis of Y-doped WS_2 by extended X-ray absorption fine structure (EXAFS) spectroscopy (Fig. 3j) show a dominant peak at 2.2 Å, indexed to the Y–S bonds in comparison with yttrium sulfide. Theoretically, the energy of 2H WS_2 is much lower than its 1T phase (>0.6 eV per formula unit). With increasing Y doping levels, the energy differences between 2H and 1T phases noticeably decrease, but it remains difficult to reverse the relative stability (Supplementary Fig. 68). Owing to the substitution of W (valency +4) in WS_2 by low-valence Y (+3), the charge densities near the Fermi level tend to be localized around Y atoms, thus going against electron transfer (Supplementary Fig. 69). Moreover, the increase of defect scattering by Y dopants would also reduce the electrical conductivity. Thus, the electrical conductivity of Y-doped WS_2 is experimentally measured to be 2.31×10^{-3} S cm^{-1}, much lower than that of pure WS_2 (8.13×10^{-2} S cm^{-1}) (Supplementary Table 3). This is in contrast to those reported for d orbital electron-enriched metal (Re, Nb)-doped MoS_2[31,32] and our Nb-doped $TiSe_2$ (Supplementary Figs. 47–50), exhibiting substantial improvements in the electrical conductivities (Supplementary Figs. 51, 70 and Supplementary Table 3).

2D heteroatoms (Y, P) co-doped WS_2 (1T)

While engineering the quaternary MAX phase $(W_{2/3}Y_{1/3})_2AlC$, other vapours such as phosphorus could be easily and simultaneously introduced into the synthetic system, creating both Y and P co-doped WS_2 (Supplementary Figs. 52–56). As illustrated by the Raman spectra (Fig. 4d), for Y, P co-doped WS_2 there are three dominant peaks at 130 cm^{-1} (J_1), 258 cm^{-1} (J_2) and 406 cm^{-1} (J_3), corresponding to the vibration modes of the 1T phase[6,33], as well as two peaks at 348 cm^{-1} and 414 cm^{-1}, indexed to the E_{2g}^1 and A_{1g} peaks of the 2H phase, respectively. The presence of the 1T phase in real space can be visualized via aberration-corrected STEM images (Fig. 4a and Supplementary
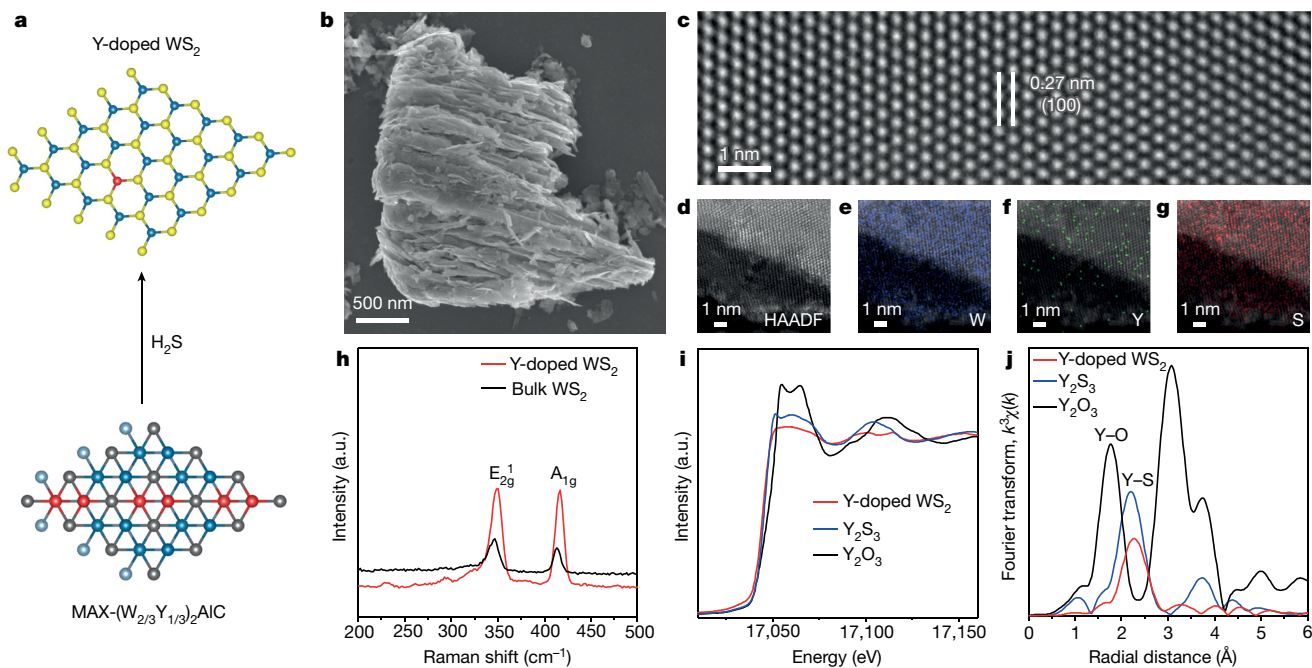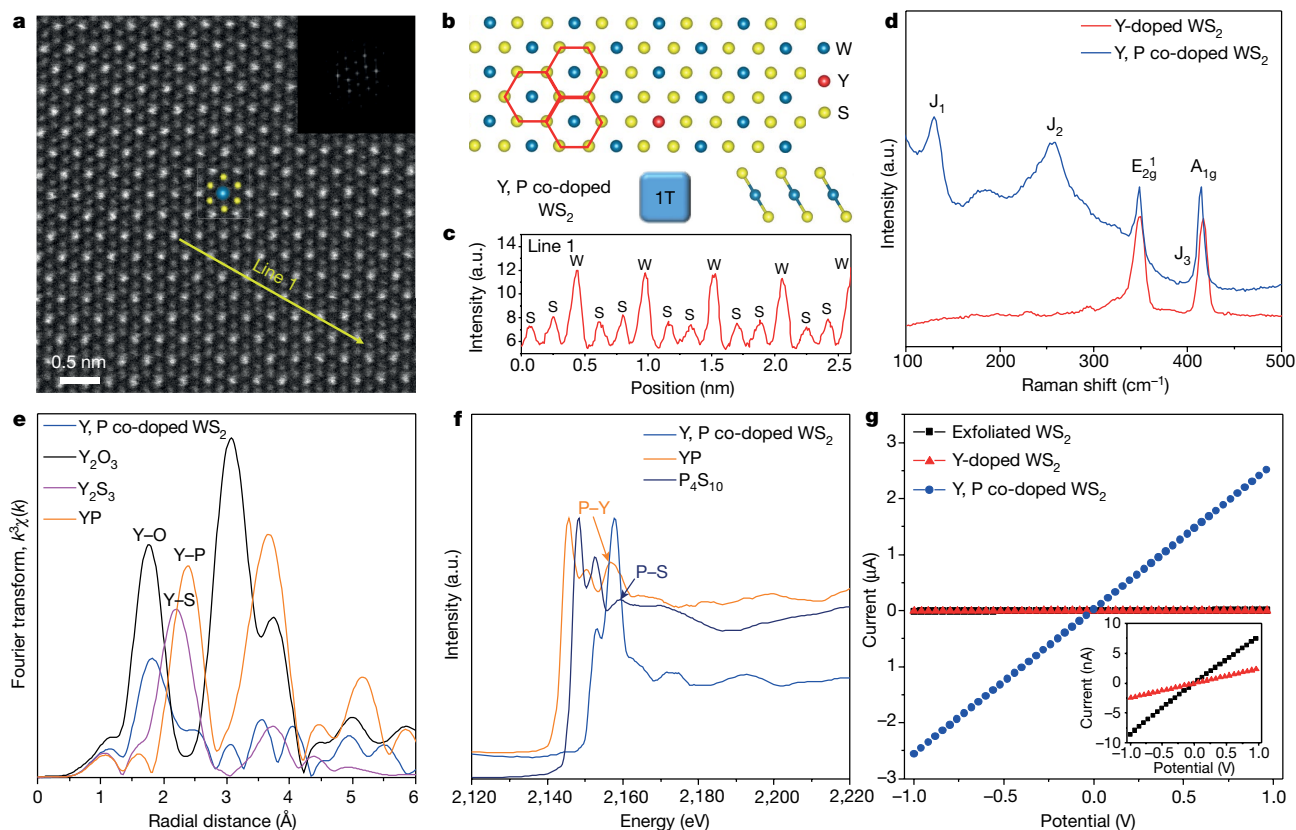
Fig. 3 | Structural characterization of 2D heteroatom-doped transition-metal chalcogenides with 2H phase derived from quaternary MAX phases. **a**, Schematic illustration of the conversion of quaternary MAX-$(W_{2/3}Y_{1/3})_2AlC$ to Y-doped WS_2. **b**, Typical scanning electron microscope image of Y-doped WS_2, showing the expanded structure. **c**, **d**, High-resolution TEM (**c**) and high-angle annular dark-field (**d**) images of Y-doped WS_2 layers. **e**–**g**, Elemental mapping images of W (**e**), Y (**f**) and S (**g**) species in Y-doped WS_2 layers. **h**, Raman spectra of Y-doped WS_2 and bulk WS_2. **i**, **j**, Y K-edge XANES spectra (**i**) and Fourier transform spectra (**j**) of Y K-edge EXAFS for Y-doped WS_2, demonstrating the presence of Y–S bonds in Y-doped WS_2.

Fig. 4 | Structural characterization and electrical properties of 2D heteroatom (Y and P) co-doped WS_2 with 1T phase derived from quaternary MAX-$(W_{2/3}Y_{1/3})_2AlC$. a, Atomic-resolution STEM image and its corresponding fast Fourier transform patterns (inset). **b**, Atomic configuration of Y, P co-doped WS_2, exhibiting the 1T phase. **c**, Line intensity profile along the highlighted arrow in **a**. **d**, Raman spectra of Y, P co-doped WS_2. **e**, Fourier transform spectra of Y K-edge EXAFS. **f**, P K-edge XANES spectra for Y, P co-doped WS_2. **g**, Current versus voltage curves of Y, P co-doped WS_2, Y-doped WS_2 and exfoliated WS_2.

Article

Fig. 57). Combined with the intensities of cation and anion sites, the S and W elements can be identified using image contrast, as shown by the line intensity profile (Fig. 4c) acquired along the highlighted arrow in Fig. 4a. All the metal W atoms are located at the centres of octahedral units, in accordance with the atomic models of the 1T phase[4,34] (Fig. 4b). Y elemental mapping images (Supplementary Figs. 58a and 59a) show that all the Y atoms are located at the centres of octahedral units, occupying the W sites in WS_2. This can be further demonstrated via the line intensity profiles (Supplementary Figs. 58c, 58e and 59c), in which the intensities of the Y sites are weaker than those of the W sites and stronger than those of the S sites, directly demonstrating the presence of Y–S bonds in Y, P co-doped WS_2. By carefully analysing the Y, P elemental mapping images and the line intensity profiles (Supplementary Figs. 58f, 58g, 59d–i), it is clear that the P atoms are located on the top of both Y and S sites, verifying the presence of Y–P and P–S bonds in the sample. These bonds can be further demonstrated via Fourier transform spectra of EXAFS (Fig. 4e and Supplementary Fig. 60), where there are two dominant peaks between 1.3 Å and 2.8 Å, corresponding to the overlap of Y–O, Y–S and Y–P bonds at 1.7 Å, 2.2 Å and 2.4 Å, respectively. In the P K-edge XANES spectra of Y, P co-doped WS_2 (Fig. 4f), there is one prominent peak centred at 2,158 eV, attributed to the overlap of P–Y bonds (2,157 eV) and P–S bonds (2,159 eV), in good agreement with the above EXAFS, aberration-corrected STEM images and the corresponding elemental mapping analysis.

Density functional theory calculations confirm that as P atoms adsorb on the hollow site 2 (h2), sulfur site 2 (S2) and tungsten site (W), the energy differences between 2H and 1T WS_2 are negligible. However, when P atoms adsorb on the top of the Y atoms and their neighbours such as hollow site 1 (h1) and sulfur site 1 (S1), the energies of the 1T WS_2 are surprisingly lower than when in the 2H phase, revealing that there is a unique yttrium–phosphorus (Y–P) joint effect that stabilizes the configuration of the 1T phase (Supplementary Figs. 71 and 72). Furthermore, it is difficult to reverse the relative energy stability between 2H and 1T WS_2 by independent Y-doping or P-adsorption (Supplementary Figs. 61 and 73). Even after storage under ambient conditions for about one year, the 1T-containing WS_2 remains stable (Supplementary Fig. 62), unlike the 1T transition-metal dichalcogenides produced via traditional methods that have poor stability at high temperatures (>573 K)[8,35]. Such Y, P co-doped WS_2 exhibits a linear current–voltage (I–V) characteristic with a low resistance of 387 kΩ per □, close to that reported for 1T′ WS_2 (430 kΩ per □)[6], three orders of magnitude lower than those of 2H Y-doped WS_2 (413 MΩ per □) and exfoliated WS_2 (124 MΩ per □) (Fig. 4g, Supplementary Fig. 63 and Supplementary Table 3).

The accordion-like structure, highly exposed surfaces and abundant 1T phase (Fig. 4d and Supplementary Fig. 64) of the resultant transition-metal dichalcogenides mean that they could be directly used as electrocatalysts for the hydrogen evolution reaction (Supplementary Figs. 65 and 66). We believe that our synthetic protocol has the potential to convert a series of non-vdW solids to 2D vdW nanocrystals with selected phases, achieving high-throughput monolayers, specific dopants and tailored electronic features, as well as broad applications in fields such as electronics, catalysis and energy storage.

Online content

Any methods, additional references, Nature Research reporting summaries, source data, extended data, supplementary information, acknowledgements, peer review information; details of author contributions and competing interests; and statements of data and code availability are available at https://doi.org/10.1038/s41586-019-1904-x.

1. Coleman, J. N. et al. Two-dimensional nanosheets produced by liquid exfoliation of layered materials. *Science* **331**, 568–571 (2011).
2. Lin, Z. et al. Solution-processable 2D semiconductors for high-performance large-area electronics. *Nature* **562**, 254–258 (2018).
3. Huang, Y. et al. Reliable exfoliation of large-area high-quality flakes of graphene and other two-dimensional materials. *ACS Nano* **9**, 10612–10620 (2015).
4. Zhou, J. et al. A library of atomically thin metal chalcogenides. *Nature* **556**, 355–359 (2018).
5. Chen, X. et al. CVD-grown monolayer MoS_2 in bioabsorbable electronics and biosensors. *Nat. Commun.* **9**, 1690–1701 (2018).
6. Voiry, D. et al. Enhanced catalytic activity in strained chemically exfoliated WS_2 nanosheets for hydrogen evolution. *Nat. Mater.* **12**, 850–855 (2013).
7. Zhu, J. et al. Argon plasma induced phase transition in monolayer MoS_2. *J. Am. Chem. Soc.* **139**, 10216–10219 (2017).
8. Eda, G. et al. Photoluminescence from chemically exfoliated MoS_2. *Nano Lett.* **11**, 5111–5116 (2011).
9. Zhang, J. et al. Single platinum atoms immobilized on an MXene as an efficient catalyst for the hydrogen evolution reaction. *Nat. Catal.* **1**, 985–992 (2018).
10. Kundu, D., Adams, B. D., Ort, V. D., Vajargah, S. H. & Nazar, L. F. A high-capacity and long-life aqueous rechargeable zinc battery using a metal oxide intercalation cathode. *Nat. Energy* **1**, 16119–16126 (2016).
11. Zhang, C. et al. High capacity silicon anodes enabled by MXene viscous ink. *Nat. Commun.* **10**, 849–857 (2019).
12. Yan, M. et al. Water-lubricated intercalation in $V_2O_5 \cdot nH_2O$ for high-capacity and high-rate aqueous rechargeable zinc batteries. *Adv. Mater.* **30**, 1703725–1703730 (2018).
13. Wang, Y. et al. In situ exfoliated, N-doped, and edge-rich ultrathin layered double hydroxides nanosheets for oxygen evolution reaction. *Adv. Funct. Mater.* **28**, 1703363–1703368 (2018).
14. Liu, J., Qian, X. & Fu, L. Crystal field effect induced topological crystalline insulators in monolayer IV–VI semiconductors. *Nano Lett.* **15**, 2657–2661 (2015).
15. Balan, A. P. et al. Exfoliation of a non-van der Waals material from iron ore hematite. *Nat. Nanotechnol.* **13**, 602–609 (2018).
16. Naguib, M. et al. Two-dimensional nanocrystals produced by exfoliation of Ti_3AlC_2. *Adv. Mater.* **23**, 4248–4253 (2011).
17. Barsoum, M. W. *MAX Phases: Properties of Machinable Ternary Carbides and Nitrides* (Wiley, 2013).
18. Sokol, M., Natu, V., Kota, S. & Barsoum, M. W. On the chemical diversity of the MAX phases. *Trends Chem.* **1**, 210–223 (2019).
19. Xuan, J. et al. Organic-base-driven intercalation and delamination for the production of functionalized titanium carbide nanosheets with superior photothermal therapeutic performance. *Angew. Chem. Int. Ed.* **55**, 14569–14574 (2016).
20. Ghidiu, M., Lukatskaya, M. R., Zhao, M. Q., Gogotsi, Y. & Barsoum, M. W. Conductive two-dimensional titanium carbide 'clay' with high volumetric capacitance. *Nature* **516**, 78–81 (2014).
21. Lukatskaya, M. R. et al. Cation intercalation and high volumetric capacitance of two-dimensional titanium carbide. *Science* **341**, 1502–1505 (2013).
22. Li, M. et al. Element replacement approach by reaction with Lewis acidic molten salts to synthesize nanolaminated MAX phases and MXenes. *J. Am. Chem. Soc.* **141**, 4730–4737 (2019).
23. Barin, I. *Thermochemical Data of Pure Substances* 3rd edn (VCH, 1995).
24. Yaws, C. L. *The Yaws Handbook of Physical Properties for Hydrocarbons and Chemicals* 2nd edn (Elsevier, 2015).
25. Winterbone, D. E. *Advanced Thermodynamics for Engineers* (Butterworth-Heinemann, 1997).
26. Naguib, M., Mochalin, V. N., Barsoum, M. W. & Gogotsi, Y. 25th anniversary article: MXenes: a new family of two-dimensional materials. *Adv. Mater.* **26**, 992–1005 (2014).
27. Anasori, B., Lukatskaya, M. R. & Gogotsi, Y. 2D metal carbides and nitrides (MXenes) for energy storage. *Nat. Rev. Mater.* **2**, 16098–16114 (2017).
28. Anasori, B. et al. Two-dimensional, ordered, double transition metals carbides (MXenes). *ACS Nano* **9**, 9507–9516 (2015).
29. Meshkian, R. et al. W-based atomic laminates and their 2D derivative $W_{1.33}C$ MXene with vacancy ordering. *Adv. Mater.* **30**, 1706409–1706416 (2018).
30. Naguib, M. et al. Two-dimensional transition metal carbides. *ACS Nano* **6**, 1322–1331 (2012).
31. Deepak, F. L. et al. Fullerene-like (IF) $Nb_xMo_{1-x}S_2$ nanoparticles. *J. Am. Chem. Soc.* **129**, 12549–12562 (2007).
32. Yang, S. Z. et al. Rhenium-doped and stabilized MoS_2 atomic layers with basal-plane catalytic activity. *Adv. Mater.* **30**, 1803477–1803483 (2018).
33. Liu, Q. et al. Stable metallic 1T-WS_2 nanoribbons intercalated with ammonia ions: the correlation between structure and electrical/optical properties. *Adv. Mater.* **27**, 4837–4844 (2015).
34. Radhakrishnan, S. et al. An insight into the phase transformation of WS_2 upon fluorination. *Adv. Mater.* **30**, 1803366–1803375 (2018).
35. Lin, Y. C., Dumcencon, D. O., Huang, Y. S. & Suenaga, K. Atomic mechanism of the semiconducting-to-metallic phase transition in single-layered MoS_2. *Nat. Nanotechnol.* **9**, 391–396 (2014).

Methods

Synthesis of MAX phases

Some MAX phases were synthesized by ball-milling of commercially available powders and subsequent calcination treatments[36-40]. Taking Mo_2GeC as an example, commercial Mo, Ge and graphite in a molar ratio of 2:1.05:1 were sealed in an agate container with agate balls and milled at 600 rpm for 20 h. The mixture was then heated at a rate of 3 K min^{-1} until it reached 1,673 K and was maintained at this high temperature for 4 h. After cooling to room temperature, the bulk was ground to produce MAX-Mo_2GeC. For other MAX phases, the details are listed in Materials and Methods in the Supplementary Information.

Synthesis of 2D transition-metal chalcogenides

Transition-metal sulfides were prepared by the reaction of MAX phases or MoB with H_2S gas at temperatures of 1,073–1,373 K. Taking a TMD-MoS_2 as an example, 300 mg of MAX-Mo_2GeC was heated at a heating rate of 10 K min^{-1} under Ar flow, and an H_2S/Ar (10 vol.% H_2S) mixture was injected when the temperature reached 1,073 K. MAX-Mo_2GeC was maintained at this temperature for 4 h, generating TMD-MoS_2. Transition metal selenides were prepared by the reaction of MAX phases, MoB and $MoSi_2$ with Se vapours at temperatures of 1,073–1,373 K. Specifically, 2 g of Se powder and 300 mg of MAX-Ti_3SiC_2 were placed in low- (973 K) and high- (1,173–1,273 K) temperature zones, respectively.

Synthesis of 2D heteroatom-doped transition-metal chalcogenides

Heteroatom-doped transition-metal chalcogenides were synthesized by the reaction of quaternary MAX phases with chalcogen-containing gases. Specifically, 300 mg of MAX-$(W_{2/3}Y_{1/3})_2AlC$ was heated at a heating rate of 10 K min^{-1} under Ar flow, and then H_2S/Ar mixture was injected when the temperature reached 1,273 K. MAX-$(W_{2/3}Y_{1/3})_2AlC$ was maintained there for 4 h to produce Y-doped WS_2. Nb-doped $TiSe_2$ was derived from MAX-$(Ti_{1/2}Nb_{1/2})_2AlC$ using the same procedures as for making TMD-$TiSe_2$.

Synthesis of 2D heteroatoms (Y and P) co-doped WS_2

Y, P co-doped WS_2 was synthesized by the reaction of MAX-$(W_{2/3}Y_{1/3})_2AlC$ with H_2S gas and P vapour at a high temperature of 1,273 K. Specifically, 300 mg of $(W_{2/3}Y_{1/3})_2AlC$ and 1 g of P were placed into two separate crucibles, where P powder was placed in a low-temperature upstream zone maintained at 873 K. $(W_{2/3}Y_{1/3})_2AlC$ was heated at a heating rate of 10 K min^{-1} under Ar flow, and then the H_2S/Ar mixture was injected when the temperature reached 1,273 K. $(W_{2/3}Y_{1/3})_2AlC$ was maintained at 1,273 K for 4 h to produce Y, P co-doped WS_2. Similarly, P-doped MoS_2 was prepared by the reaction of MAX-Mo_2GeC with H_2S gas and P vapour at a high temperature of 1,073 K.

Synthesis of P-doped WS_2

P-doped WS_2 was synthesized by the reaction of bulk WS_2 with P vapour at high temperature. Specifically, 300 mg of WS_2 powders were put in a porcelain boat with 1 g of P at the upstream zone. Then the boat was heated to 1,273 K at a heating rate of 10 K min^{-1} under Ar flow and kept there for 30 min to generate P-doped WS_2.

Fabrication of thin films of Y, P co-doped WS_2, Y-doped WS_2 and exfoliated WS_2

Y, P co-doped WS_2 thin film was fabricated by vacuum filtration of Y, P co-doped WS_2 nanosheets on nylon membrane filters, which were acquired by a facile liquid exfoliation of accordion-like Y, P co-doped WS_2 in an isopropyl alcohol solvent[1]. Other thin films of Y-doped WS_2, WS_2, Nb-doped $TiSe_2$ and $TiSe_2$ were similarly obtained.

Characterization

The morphology and microstructure of materials were characterized by scanning electron microscopy (Zeiss MERLIN Compact), transmission electron microscopy (JEOL 2100F), spherical aberration-corrected transmission electron microscopy (FEI Titan G2) and X-ray diffraction (Rigaku D/MAX2200pc). Raman spectra were recorded on a Renishaw inVia Microscopic confocal Raman spectrometer using a 532-nm laser beam. X-ray photoelectron spectroscopy was recorded by a Thermo Electron ESCALAB 250 XPS spectrometer. Atomic force microscopy measurements were carried out on a Dimension ICON scanning probe microscope (Veeco/Bruker). X-ray absorption near-edge fine structure (XANES) and extended X-ray absorption fine structure (EXAFS) data for the Y K-edge were collected on BL14W1 and BL1W1B at the Shanghai Synchrotron Radiation Facility and the Beijing Synchrotron Radiation Facility, respectively. XANES data for the P K-edge were collected on BL4B7B at the Beijing Synchrotron Radiation Facility. Current-versus-voltage measurements were conducted using the two-electrode method on an electrochemical workstation (CHI760E, CH Instruments) in a voltage range of −1 V to 1 V at a scan rate of 10 mV s^{-1}. The electrical conductivities of powder samples were investigated on a four-probe powder resistivity tester (ST2722-SZ, Suzhou Jingge Electronic Co., Ltd).

Vapour pressure calculations

With the aid of log K_f values for two-phase equilibria solid–gas or liquid–gas ($AZ_{sol,liq}$–AZ_{gas}), we calculated the vapour pressures of AZ gases according to the following equation[23]:

$$\log K = \log K_f(AZ_{gas}) - \log K_f(AZ_{sol,liq}) = \log[p(AZ_{gas})/a(AZ_{sol,liq})]$$

where p is the vapour pressure, a is the activity of AZ in the condensed phase, K_f is the equilibrium constant of formation reaction and log K_f values taken from the literature[23] are partially listed in Supplementary Tables 4–7. In general, $a = 1$ for pure substances in a condensed phase.

For the evaporation equation of pure substances at a given temperature T:

$$\log K_f(AZ_{gas}) - \log K_f(AZ_{sol,liq}) = \log p(AZ_{gas})$$

and

$$p(AZ_{gas}) = 10^{\log K_f(AZ_{gas}) - \log K_f(AZ_{sol,liq})}$$

where p is in units of bar (1 bar $= 10^5$ Pa). Taking $1/T$ and ln p as the horizontal and vertical axis respectively, linear curves were made as shown in Supplementary Fig. 6. According to the Clausius–Clapeyron equation[25]:

$$\ln p = -\Delta H_m/(RT) + C \tag{1}$$

where p is vapour pressure, ΔH_m is molar enthalpy of evaporation, R is molar gas constant and C is a constant, these linear curves confirm that the Clausius–Clapeyron equation can be applied to evaluate the relationship between vapour pressure and temperature.

In the case of AZ substances that lack log K_f values in the literature, the boiling point and the corresponding vapour pressure (1 atm $= 101,325$ Pa) are selected to evaluate the relationship between vapour pressure and temperature (Supplementary Table 8)[24].

Data availability

The data that support the findings of this study are available from the corresponding authors on reasonable request.

36. Sun, Z. M. Progress in research and development on MAX phases: a family of layered ternary compounds. *Int. Mater. Rev.* **56**, 143–166 (2011).
37. Barsoum, M. W. The $M_{N+1}AX_N$ phases: a new class of solids: thermodynamically stable nanolaminates. *Prog. Solid State Chem.* **28**, 201–281 (2000).
38. Eklund, P., Beckers, M., Jansson, U., Hogberg, H. & Hultman, L. The $M_{n+1}AX_n$ phases: materials science and thin-film processing. *Thin Solid Films* **518**, 1851–1878 (2010).

Article

39. Magnuson, M. & Mattesini, M. Chemical bonding and electronic-structure in MAX phases as viewed by X-ray spectroscopy and density functional theory. *Thin Solid Films* **621**, 108–130 (2017).
40. Naguib, M. et al. New two-dimensional niobium and vanadium carbides as promising materials for Li-ion batteries. *J. Am. Chem. Soc.* **135**, 15966–15969 (2013).

Author contributions S.Y., S.L. and P.M.A. supervised the project. S.Y. and Z.D. designed and carried out all of the experiments. S.Z. and X.Z. carried out the density functional theory calculations. S.W. and B.L. performed the scanning electron microscope, TEM and X-ray diffraction measurements. B.L. carried out the X-ray photoelectron spectroscopy and Raman analysis. L.S. contributed to the XANES and EXAFS measurements. Z.D. performed the atomic force microscopy. Z.D. and Y.G. designed the film electrodes and carried out the electrical and electrocatalytic measurements. All authors discussed the results and assisted during manuscript preparation.